Combined Effects of Wind-Driven Upwelling and Internal Tide on the Continental Shelf

A. L. KURAPOV, J. S. ALLEN, AND G. D. EGBERT

College of Oceanic and Atmospheric Sciences, Oregon State University, Corvallis, Oregon

(Manuscript received 13 November 2008, in final form 1 September 2009)

ABSTRACT

Internal tides on the continental shelf can be intermittent as a result of changing hydrographic conditions associated with wind-driven upwelling. In turn, the internal tide can affect transports associated with upwelling. To study these processes, simulations in an idealized, alongshore uniform setup are performed utilizing the hydrostatic Regional Ocean Modeling System (ROMS) with conditions corresponding, as closely as possible, to the central Oregon shelf. ''Wind only'' (WO), ''tide only'' (TO), and ''tide and wind'' (TW) solutions are compared, utilizing cases with constant upwelling-favorable wind stress as well as with time-variable observed stress. The tide is forced by applying cross-shore barotropic flow at the offshore boundary with intensity sufficient to generate an internal tide with horizontal velocity amplitudes near 0.15 m s^{-1}, corresponding to observed levels. The internal tide affects the subinertial circulation, mostly through the changes in the bottom boundary layer variability, resulting in a larger bottom stress and a weaker depth-averaged alongshore current in the TW case compared to WO. The spatial variability of the cross-shore and vertical volume transport is also affected. Divergence in the Reynolds stress associated with the baroclinic tidal flow contributes to the tidally averaged cross-shore momentum balance. Internal waves cause high-frequency variability in the turbulent kinetic energy in both the bottom and surface boundary layers, causing periodic restratification of the inner shelf in the area of the upwelling front. Increased vertical shear in the horizontal velocity resulting from the superposition of the upwelling jet and the internal tide results in intermittent patches of intensified turbulence in the mid–water column. Variability in stratification associated with upwelling can affect not only the propagation of the internal tide on the shelf, but also the barotropic-to-baroclinic energy conversion on the continental slope, in this case changing the classification of the slope from nearly critical to supercritical such that less barotropic tidal energy is converted to baroclinic and a larger fraction of the baroclinic energy is radiated into the open ocean.

1. Introduction

A narrow coastal shelf off Oregon, along the U.S. west coast, is an area of energetic baroclinic alongshore current and coastal upwelling driven by predominantly southward wind in summer. The associated surface alongshore velocity is on average near 0.5 m s^{-1} and can reach 1 m s^{-1} during events of intensified wind. Due to upwelling, a horizontal cross-shore density gradient develops in shelf waters. In agreement with the thermal wind balance, the alongshore jet is vertically sheared, with a weaker current near the bottom. While the fundamentals of upwelling dynamics are well understood (Allen et al. 1995), the potential effects of the internal tide on the coastal ocean circulation are relatively less studied. The dominant tidal constituent off of Oregon is M_2 with surface elevation amplitudes near 0.8 m and barotropic tidal currents near 5 cm s^{-1} on the shelf. Vertical motions associated with the barotropic tidal flow over sloping bathymetry cause baroclinic displacements of isopycnal surfaces at the tidal frequency, forcing the internal tide (e.g., Gill 1982; Baines 1982). Analysis of moored velocity time series data suggests that the M_2 internal tide on the Oregon shelf has a vertical structure related to the first baroclinic mode and is often surface amplified, with baroclinic velocities near 10–15 cm s^{-1} (Hayes and Halpern 1976; Torgrimson and Hickey 1979; Erofeeva et al. 2003). Up to 50% of the horizontal velocity variance can be contained in the tidal frequency band (see Erofeeva et al. 2003). Thus, near the surface, the internal tide motions can provide a significant fraction of the ocean energetics. Near the bottom, where currents associated with wind forcing are

Corresponding author address: A. Kurapov, College of Oceanic and Atmospheric Sciences, Oregon State University, 104 COAS Admin. Bldg., Corvallis, OR 97331-5503.
E-mail: kurapov@coas.oregonstate.edu

DOI: 10.1175/2009JPO4183.1

relatively lower, the internal tide can possibly dominate the current variability.

Historically, wind-driven and tidal flows on the Oregon shelf have been studied separately. Using nonlinear primitive equation hydrostatic models, different aspects of the wind-driven flows relevant to the Oregon shelf have been investigated (e.g., Allen et al. 1995; Federiuk and Allen 1995; Allen and Newberger 1996; Oke et al. 2002; Wijesekera et al. 2003; Gan et al. 2005; Kurapov et al. 2005; Springer et al. 2009). Barotropic tides in this area have been modeled by Erofeeva et al. (2003) with assimilation of satellite and in situ observations in a linear shallow water model. To obtain estimates of the M_2 internal tide on the central Oregon shelf, Kurapov et al. (2003) assimilated surface velocity observations from high-frequency (HF) radars in a model that described harmonic linear oscillations of the stratified ocean with respect to the state of rest (no background currents, horizontally uniform background stratification). Estimates of tidal harmonic constants obtained in a series of overlapped time windows revealed internal tide intermittency that was consistent with that observed at a midshelf mooring. In that study, it was noted that during a period of intensified alongshore wind, results were more accurate if the tidal velocity estimates from surface HF radar data at distances <20 km from the coast were excluded from the assimilation. It was hypothesized that those observations could have provided useful information if the model were improved by allowing horizontally variable background stratification and the sheared alongshore current, associated with upwelling.

Surprisingly little research has been done on how wind-driven and internal tidal shelf flows influence each other. One of the most focused studies on this subject dates back to the Ph.D. thesis by Mooers (1970), who used the method of characteristics to solve a wave equation in a two-dimensional (2D) setup (cross-shore and vertical coordinates) to study internal wave propagation through a frontal zone in a coastal upwelling region (Mooers 1975a,b). In particular, he found that a significant asymmetry in the upgoing and downgoing characteristics is introduced when the slope of the isopycnals is comparable to the slope that the characteristics would have without the frontal interaction. Among more recent relevant studies, Chen et al. (2003) modeled and analyzed the internal tide in the presence of a tidal front, in an idealized, cross-shore, configuration relevant to the U.S. east coast. Park and Watts (2006) used data from an array of pressure-sensor-equipped inverted echo sounders and found that changes in background ocean conditions can cause variations in the internal tide energy levels. Pereira et al. (2007) utilized a three-dimensional (3D) model to study the dynamics in the South Brazil Bight and found that the Brazil Current affects the structure of the internal tides in the area, acting in part as a barrier to their onshore propagation. They also found that internal tides enhanced mixing on the inshore side of the coastal current. Hall and Davies (2007) simulated internal tides off the west coast of Scotland and found that both upwelling- and downwelling-favorable winds change the energetics of internal tides over the shelf break area. They suggested that those changes could be associated with changes in stratification along the continental slope and in the surface boundary layer. Observational analysis by Avicola et al. (2007) suggested that turbulence patches found over the shelf in the middle of the water column, away from surface and bottom boundary layers, can be caused by the combined shear from the wind-driven alongshore current and the internal tide.

While the effects of the relatively slowly changing background hydrographic conditions on internal tide propagation have been documented, it remains largely unknown whether and how the internal tide affects coastal transports on relatively slower temporal scales.

Here, we present the results of simulations of the wind-driven coastal upwelling and internal tide in combination, run in a 2D, cross-shore model. The main focus is on whether and how the internal tide changes alongshore, cross-shore, and vertical transports as well as the variability in the turbulence fields, in comparison to previously studied cases without tides (see Allen et al. 1995, Wijesekera et al. 2003). We also provide analysis of the internal tide energetics over the continental slope and shelf to better understand intermittency in the internal tide.

2. Model

Computations are performed with the Regional Ocean Modeling System (ROMS; information online at www.myroms.org), based on free-surface, hydrostatic, Boussinesq primitive equations and utilizing efficient and accurate numerical algorithms (Shchepetkin and McWilliams 2005). To represent the physics on subgrid scales, the Mellor–Yamada 2.5 turbulence scheme is used (Mellor and Yamada 1982; see also Wijesekera et al. 2003). A quadratic bottom stress formulation is utilized. The 2D solutions (varying in the cross-shore and vertical directions, and uniform in the alongshore direction) are obtained by running the model in a short south-to-north periodic channel with alongshore uniform bathymetry, forcing, and other conditions. Cases discussed in the following sections are designed to be relevant to summer wind-driven upwelling off Oregon, with the Coriolis parameter $f = 10^{-4}\ \mathrm{s}^{-1}$. Cartesian coordinates are

introduced with the x axis directed toward the coast, y axis north, and z axis upward. The cross-shore u and alongshore v components of the horizontal velocity are projections in the x and y directions, respectively. Note that ROMS equations are derived by transformation from Cartesian z to terrain-following s coordinates, which allows for the resolution of the surface and bottom boundary layers over the shelf and slope. After discretization, the lowest s surface is defined at the bottom, $z = -H(x)$, and the upper s surface at the free surface, $z = \zeta(x, t)$; the positions and thicknesses of the s layers vary with time (see Shchepetkin and McWilliams 2005).

The ocean bottom profile, $H(x)$, is obtained as the alongshore average of the bathymetric data off the Oregon coast between 45.05° and 45.20°N, with a maximum depth of 1000 m (Fig. 1). We deliberately included several small-scale bathymetric features on the slope to allow more effective baroclinic tide generation by the cross-shore barotropic tidal flow. The resolution is 250 m in the horizontal and 120 (section 3) or 60 (section 4) layers in the vertical. Near-surface and bottom layers are resolved relatively better. All analyses have been performed using hourly model outputs.

The depth-averaged currents, denoted with an overbar, are referred to as barotropic and deviations from the depth-averaged currents as baroclinic; for example,

$$u = \overline{u} + u_{\mathrm{bc}}. \tag{1}$$

The time series fields are split into the subtidal (low pass filtered) and high-frequency (high-pass filtered) components; for example,

$$u = \langle u \rangle + u', \tag{2}$$

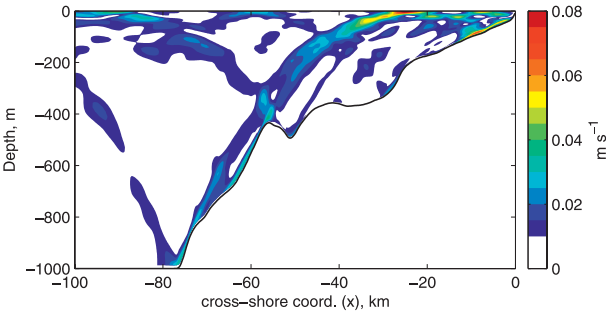

FIG. 1. Baroclinic tidal KE$^{1/2}$ (4), estimated for the interval $t = (-3, 0)$ days (the TO case).

where the subtidal component $\langle u \rangle$ is obtained by applying a 40-h half-amplitude filter.

No-normal-flow and free-slip boundary conditions are applied at the coast ($x = 0$). At the offshore boundary ($x = -200$ km), the Flather condition (Flather 1976) is utilized for the depth-averaged cross-shore velocity $\overline{u}$:

$$\overline{u} = U_0 \sin[\omega(t - t_0)] - \sqrt{\frac{g}{H}}\zeta, \tag{3}$$

where $\omega = 2\pi/12.42$ h^{-1} is the M_2 frequency, g the gravitational acceleration, and t_0 the initial time. Passive radiation boundary conditions are applied for all the other variables, including ζ, u, v, temperature T, and salinity S.

Cases driven by the tide and wind stress in combination (TW) and by the wind stress only (WO) will be considered. Periods of time at the beginning of the TW runs, when only tidal forcing is applied, will be referred to as case TO.

The forcing amplitude $U_0 = 0.2$ m s^{-1} is chosen to be large enough to produce internal tide currents on the

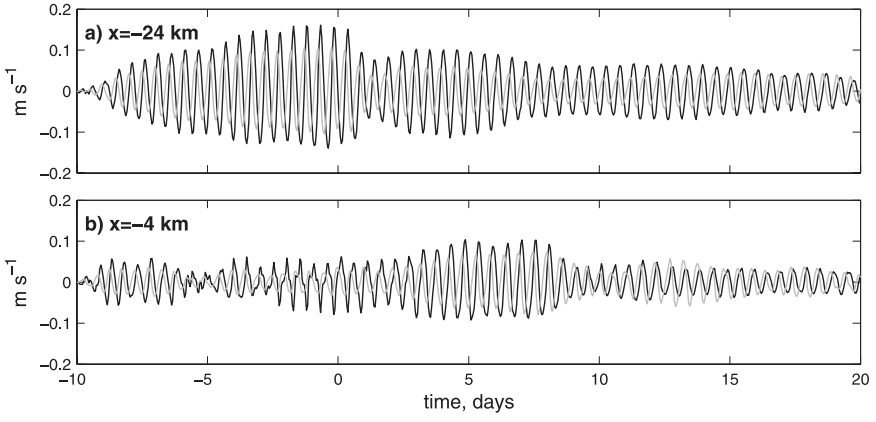

FIG. 2. Time series of the high-pass-filtered baroclinic velocity components at the surface (u'_{bc}, black; v'_{bc}, halftone) (a) in the area of tidal beam reflection ($x = -24$ km, $H = 208$ m) and (b) near the coast ($x = -4$ km, $H = 60$ m).

shelf with maximum amplitudes near observed values of 0.1–0.15 m s^{-1}. Note that ζ in (3), which is determined by the interior dynamics, is near 2 m and the typical barotropic tidal currents in the domain interior are near 0.02 m $s^{-1} \ll U_0$. Although these barotropic tidal features differ from those actually observed off Oregon, we will show that energetics and variability in the baroclinic tide are representative of this area. Note that in a more realistic, 3D case the internal tide would be generated as a result of barotropic flow over variable bathymetry in both the alongshore and cross-shore directions. A larger tidal sea surface elevation variation is needed for our study in part because in the 2D case the internal tide is generated only by the cross-shore component of the barotropic tidal current.

3. Cases with constant wind stress

Case TW begins at $t_0 = -10$ days and runs for a total of 30 days. It starts from a state of rest, with horizontally uniform initial T and S corresponding to the average conditions off the mid–Oregon shelf in April (Smith et al. 2001). During the first 10 days, $t = (-10, 0)$, only tidal forcing is applied. During the first 7 days of simulation, the magnitude of the internal tide is increased gradually until the internal tide reaches a quasi-equilibrium state (Fig. 2). The exact equilibrium cannot be achieved in part because the internal tide mixes water near bottom on the shelf, changing the background stratification. However, after $t = -3$ days, the intensity of the internal tide and the beamlike structure of the zones of increased tidal kinetic energy (see section 3a) remain very similar, as verified in a run for an extended period of 20 days forced by tides alone.

Beginning at $t = 0$, spatially uniform atmospheric forcing is applied. Both the wind stress and heat flux are ramped up over a 2-day period (using a cosine-shape function) from 0 to -0.05 N m^{-2} and 200 W m^{-2}, respectively, and then held constant. Case WO starts at $t = 0$ from rest, using the same initial stratification, and is run for 20 days with the same wind stress and heat flux as in the TW case.

Figure 3 shows cross-shore sections of the daily averaged alongshore velocity and potential density σ_θ for the TW case, with averaging over intervals of $t = (-1, 0)$, (4, 5), (9, 10), (14, 15), and (19, 20), referred to as days 0, 5, 10, 15, and 20, respectively. The wind stress forces the development of a sheared southward coastal jet with the core moving progressively offshore. The offshore Ekman transport in the surface boundary layer is balanced by the onshore transport of near-bottom denser water. For instance, contour $\sigma_\theta = 26$ kg m^{-3}, initially at a depth of 120 m, is about to outcrop near the surface by

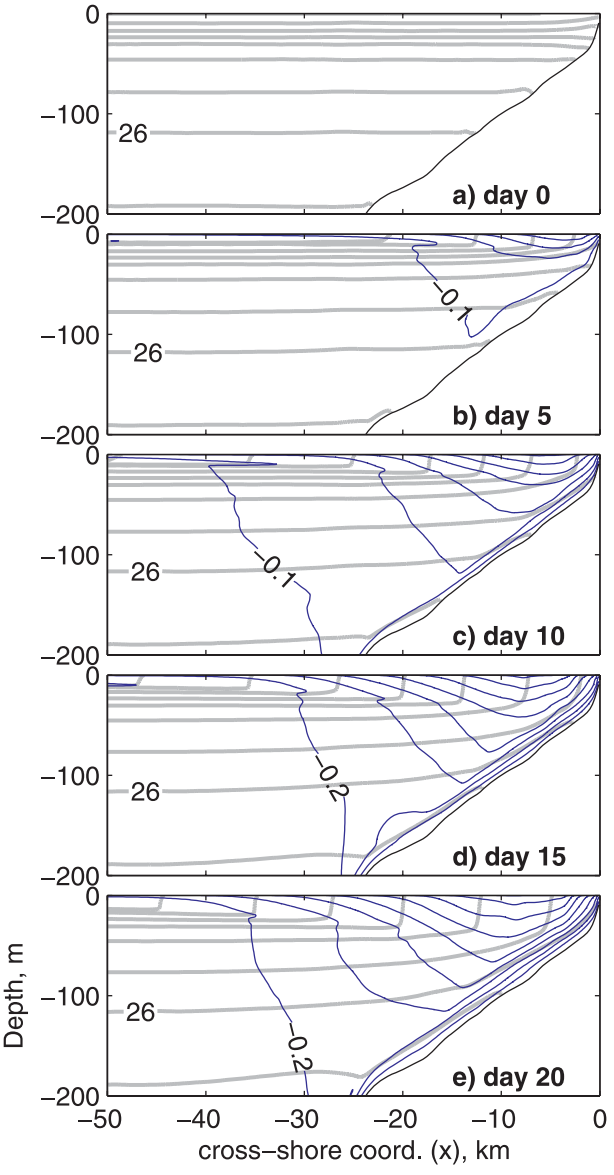

FIG. 3. Daily averaged potential density (thick halftone contour lines, every 0.5 kg m^{-3}) and alongshore velocity (thin dark contours, every 0.1 m s^{-1}), for the TW case on (top to bottom) days 0, 5, 10, 15, and 20.

day 20. Next, we analyze the effects associated with the internal tide evolving in the presence of this time-variable background.

a. Internal tide variability

To show the spatial distribution of the zones of the intensified internal tide, we compute estimates of the tidal baroclinic kinetic energy (KE) per unit mass averaged over a tidal cycle:

$$\mathrm{KE} = \frac{1}{4}(|\mathbf{u}_{\mathrm{bc}}|^2 + |\mathbf{v}_{\mathrm{bc}}|^2), \tag{4}$$

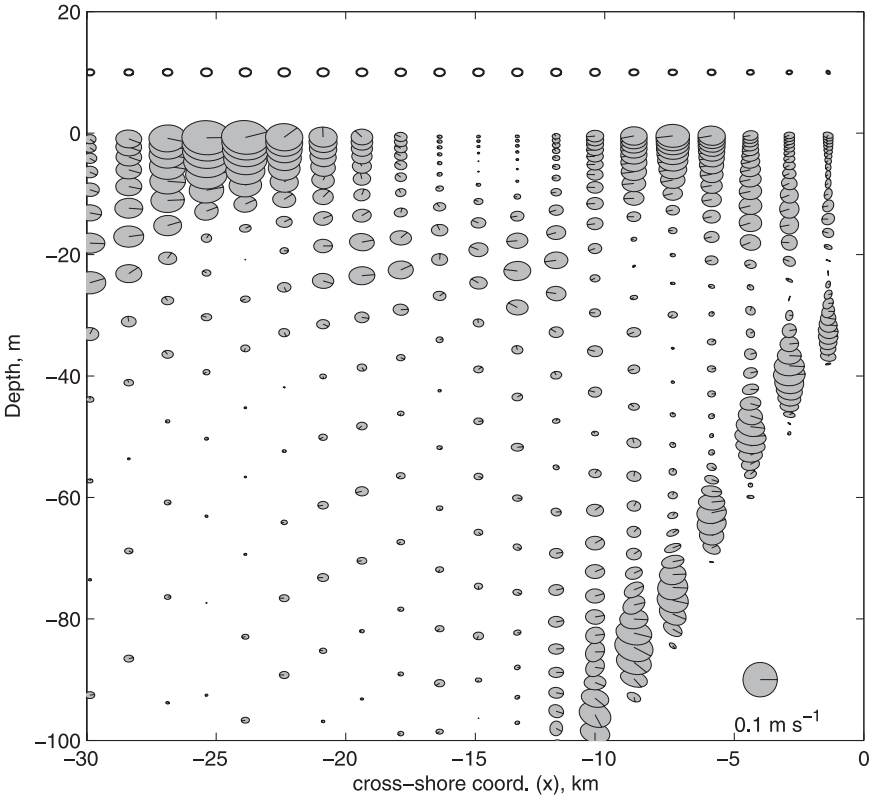

FIG. 4. Barotropic (shown above 0-m depth) and baroclinic M_2 tidal horizontal velocity ellipses, resulting from harmonic analysis over the period $t = (-3, 0)$ (the TO case). The ellipses are shown for each sixth grid point in the horizontal and the fourth point in the vertical. The scale circle (bottom-right corner) corresponds to 0.1 m s^{-1}. Lines originating from the ellipses' centers denote the direction of the velocity vector at zero phase.

where $\mathbf{u}_{bc}(x, z)$ and $\mathbf{v}_{bc}(x, z)$ are complex amplitudes of M_2 tidal harmonic oscillations of the two components of the baroclinic velocity, obtained by harmonic analysis of the corresponding high-pass-filtered time series $u'_{bc}(x, z, t)$ and $v'_{bc}(x, z, t)$ in a given interval. To analyze the internal tide intermittency, we would like to perform a harmonic analysis over a series of short time intervals. However, to allow separation of the M_2 tidal and inertial (period of 17 h) harmonics, these intervals are chosen to be ≥3 days. In cases described in this section, the inertial motions are very low. However, in cases with a realistically varying wind stress (section 4), the tidal and inertial motions can be of comparable magnitude.

The plot of $KE^{1/2}$, or the RMS tidal velocity, corresponding to an interval of $t = (-3, 0)$ (see Fig. 1) provides information on the spatial structure of the internal tide not influenced by wind-driven flow (i.e., case TO). Zones of higher baroclinic tidal velocities are organized in beams that originate at topographic features with a bathymetric slope of dH/dx that is nearly critical (i.e., close to the slope of the internal wave characteristics; see, e.g., Gill 1982):

$$\tan\varphi = \sqrt{\frac{\omega^2 - f^2}{N^2 - \omega^2}}. \tag{5}$$

Here, φ is the angle that the characteristics make with the horizontal, and N is the background buoyancy frequency. The beams are less steep at shallower depths, where the background stratification is stronger (Holloway 2001). Some internal tide energy propagates into the open ocean, and some onto the shelf, where the baroclinic tide variability is influenced by beams originated over several topographic features and reflected at the surface.

Another way to look at the baroclinic tide's spatial variability is to plot M_2 barotropic and baroclinic tidal horizontal velocity ellipses (e.g., as shown over the shelf in Fig. 4), for the same interval, $t = (-3, 0)$. The barotropic tidal current is approximately 0.02 m s^{-1}. Note that off the Oregon coast, the M_2 barotropic tide propagates as a Kelvin wave, with ellipses strongly polarized in the alongshore direction (see Erofeeva et al. 2003). These dynamics are not represented in our 2D cross-shore solution and the barotropic tidal ellipses, shown in Fig. 4, are not a realistic representation of the barotropic

tide off Oregon. However, the structure of the baroclinic tide on the shelf is qualitatively similar to that found in the observations on the Oregon shelf (see Erofeeva et al. 2003; Kurapov et al. 2003), with weakly polarized ellipses, predominantly first mode structure (higher amplitudes and opposite phases near the surface and bottom), clockwise velocity vector rotation (when looking from the above), and magnitudes on the order of 0.1 m s^{-1} or weaker. Because of the intermittency of the internal tide, harmonic analysis can underestimate the tidal velocity magnitudes. For that reason, we have also looked at the time series of u'_{bc} and v'_{bc} at locations of intensified internal tides to verify that the harmonic estimates are consistent with the instantaneous high-pass-filtered velocity values (see Fig. 2).

The close-up plot of $KE^{1/2}$ in the shelf area, for the time interval $t = (-3, 0)$, is shown in Fig. 5a. The maximum RMS baroclinic tidal velocities are close to 0.1 m s^{-1} near the surface at a distance of 20–30 km from the coast, where the energetic beam that originated over the continental slope is reflected from the surface, and near the bottom on the midshelf ($H < 100$ m), where the beam is reflected upward and onshore, nearly parallel to the bottom slope. After the internal tide reaches a quasi-equilibrium state and before the wind forcing is applied (case TO, $-3 < t < 0$ days), isopycnal surfaces obtain approximately 5-m displacements that propagate onshore as internal waves and become amplified in the vicinity of the shelf slope (Fig. 6a).

The changes in the subtidal hydrographic conditions affect the baroclinic tidal KE (Figs. 5b–d). For instance, with the development of upwelling, the tidal KE is reduced at shallow depths where the tidal beam is reflected from the surface (in the vicinity of $x = -25$ km). The velocity time series analysis (see Fig. 2a) also shows a decrease in tidal amplitudes at that location associated with the onset of upwelling, although this effect is not uniformly extended to all near-surface locations (Fig. 2b). In both time series plots, irregular low-frequency modulations in the tidal velocity magnitudes are apparent. The reduction in the near-surface baroclinic tidal KE can be associated with increased dissipation in the surface boundary layer as well as changes in the level of baroclinic internal tide energy generated over the slope and propagated onto the shelf, as will be discussed in section 4.

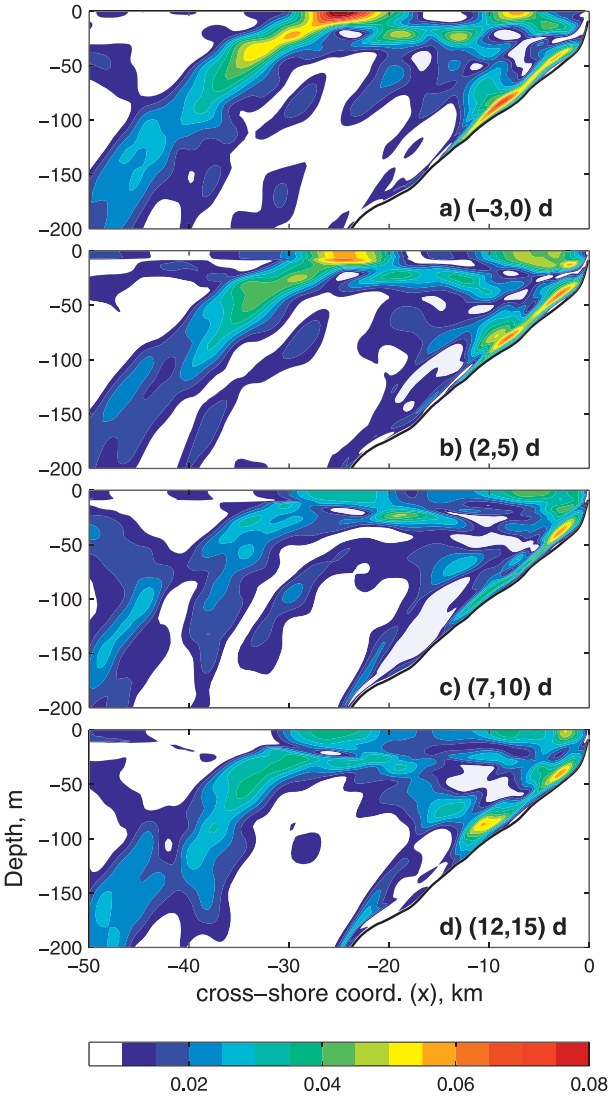

FIG. 5. Tidal baroclinic $KE^{1/2}$ (m s^{-1}), for the TW case, estimated in a series of 3-day time intervals.

b. *Tidal effect on the alongshore transport*

The internal tide influences the coastal dynamics on subinertial time scales. For instance, Figs. 7a–d shows cross-shore plots of the barotropic alongshore current $\bar{v}$ averaged in time over 5, 10, 15, and 20 days. The speed of the jet core can be smaller in the TW case than in WO by as much as 5 cm s^{-1} (or 10% of the maximum speed). Time series of subtidal $\langle \bar{v} \rangle$ at three shelf locations (Figs. 8a–c) also show a weaker current in the TW case throughout the study period. The reason for this reduction can be understood by analyzing the terms in the depth-integrated, low-pass-filtered alongshore momentum equation:

$$\langle D\bar{v} \rangle_t = -\langle D\overline{uv} \rangle_x - f\langle D\bar{u} \rangle + \langle \tau^s \rangle - \langle \tau^b \rangle, \qquad (6)$$

where $D = \zeta + H$ is the total depth; τ^s and τ^b are the surface and bottom stress per unit mass, respectively; and subscripts denote partial derivatives. In both cases, τ^s is the same. The Coriolis term is small, since $\langle D\bar{u} \rangle \approx 0$

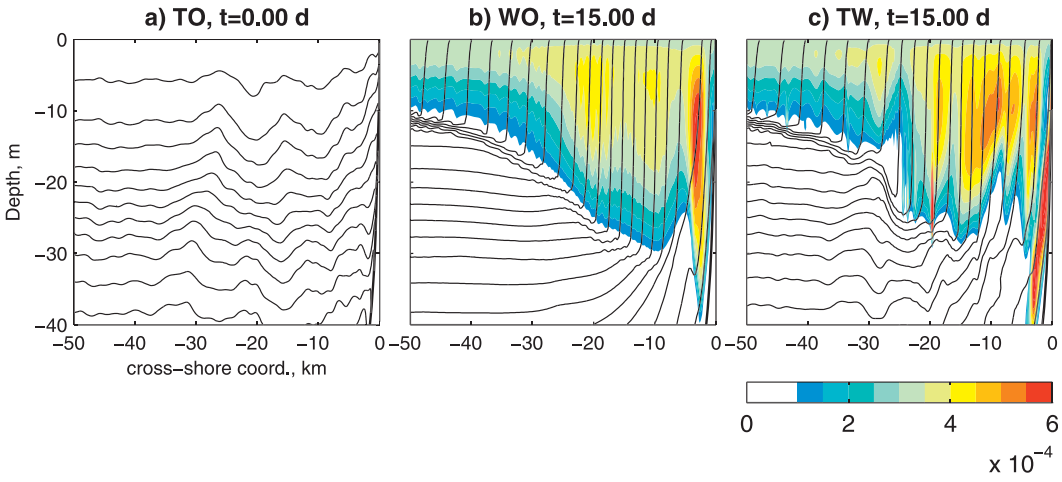

FIG. 6. Contours of instantaneous σ_θ (lines, every 0.5 kg m^{-3}) and TKE (m^2 s^{-2}, color): (a) TO, t = 0.0 days, (tides, no wind); (b) WO, t = 15.0 days; and (c) TW, t = 15.0 days.

near the coast. It might be anticipated that the subtidal bottom stress $\langle \tau^b \rangle$ would be relatively larger in the TW case (Rooth 1972), causing a smaller negative tendency and a lower current in the upwelling spinup simulation. In Figs. 8d–f, we show, at the same three locations, time series of the tendency terms $\langle D\overline{v} \rangle_t$ and in Figs. 8g–i we show the bottom stress for the two cases, all normalized by the local H. Apparently, periods of a relatively larger bottom stress correlate with those of smaller southward acceleration. To emphasize this effect, in Figs. 8j–l, we plot the time series of the differences in the tendency terms, the WO case minus TW (solid line) and the difference in $\langle \tau^b \rangle$, the TW case minus WO, all divided by local H. Indeed, these differences are positively correlated. Also, the magnitudes of the differences are comparable, suggesting that the increased bottom friction contributes to the slower current in the TW case. We will see later that the advection term can also contribute to the subtidal alongshore momentum balance (section 3c).

To further explore the effects of the internal tide on subtidal alongshore transport, we analyze vertical profiles of daily averaged v, $(\partial v/\partial z)^2$, and N^2 at the same three shelf locations (Fig. 9). On the midshelf (profiles at 10 and 6 km from the coast), the difference in subtidal v is mostly due to the differences in $\partial v/\partial z$ near the bottom. As seen both in profiles of v (Figs. 9a–d) and $(\partial v/\partial z)^2$ (Figs. 9e–h), the magnitude of the vertical shear is larger at the vertical distance of 0–20 m from the bottom in the WO case (halftone lines) than in the TW case (black lines). At the same time, the vertical extent of the layer of increased shear (the depth of the bottom boundary layer) is larger in the TW case. Profiles of daily averaged N^2 (Figs. 9i–l) are also influenced by the tides. In the WO case, the vertical stratification near bottom increases with the development of upwelling as an effect of the cross-shore Ekman buoyancy transport (Lentz and Trowbridge 1991; MacCready and Rhines 1993). In the TW case, this effect is distributed over a larger layer. In the lower (upper) part of that layer, the strength of the stratification is relatively weaker (stronger) in the TW case. These results suggest that tides introduce additional mixing and reduce stratification near the bottom. At the same time, the upslope Ekman buoyancy transport is distributed over a relatively thicker layer in the TW case. These conclusions are additionally supported by the analysis of profiles of the daily averaged turbulent

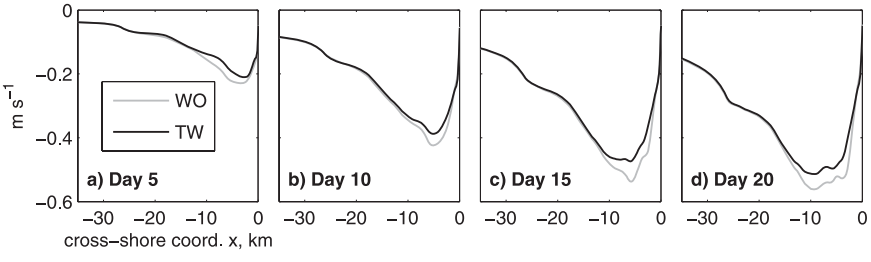

FIG. 7. Daily averaged, depth-averaged alongshore velocity on (left to right) days 5, 10, 15, and 20, for the WO (halftone) and TW (black) cases.

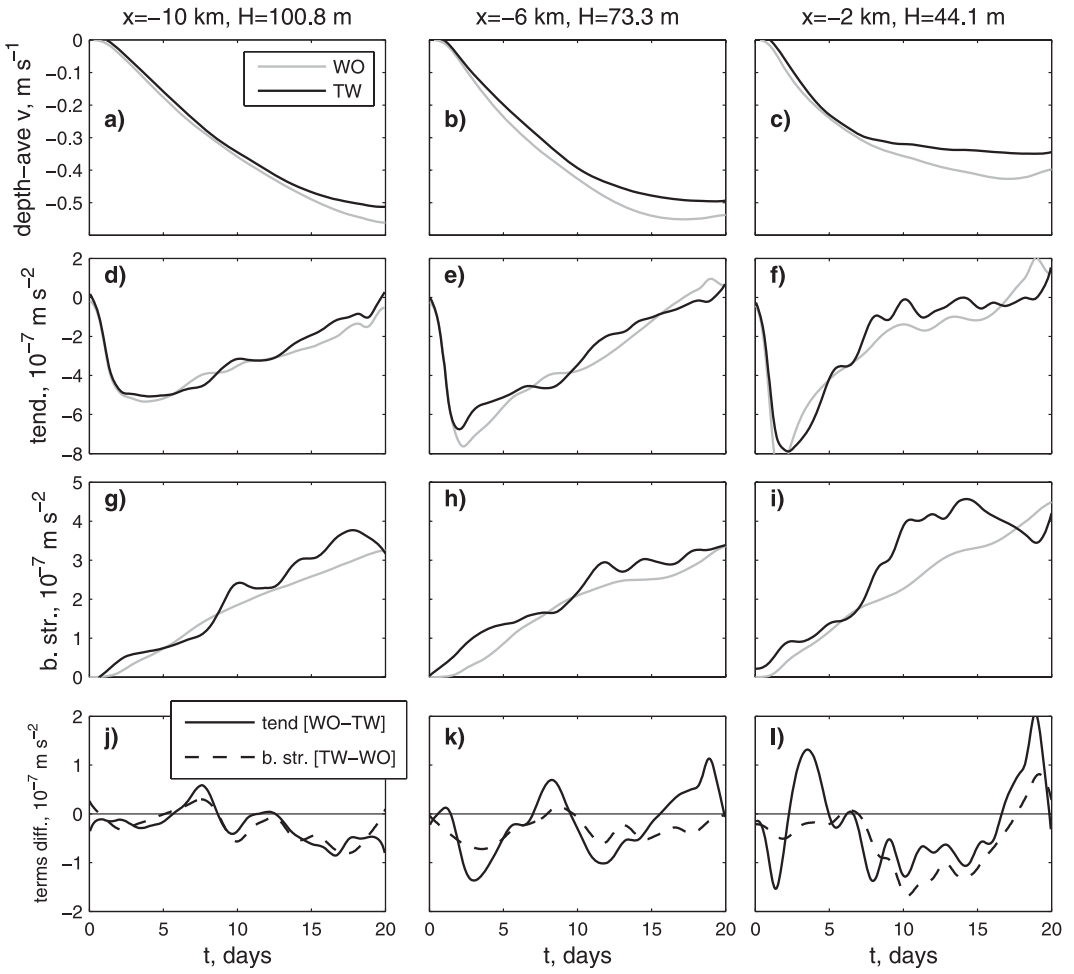

FIG. 8. Time series at three locations, (left to right) $x = -10$, -6, and -2 km, of (top) the depth-averaged subtidal alongshore velocity component $\langle \bar{v} \rangle$, for the WO and TW cases, (second from top) the tendency term $(1/H)\langle D\bar{v} \rangle_t$ in (6), (second from bottom) the bottom stress $\langle \tau^b \rangle / H$, and (bottom) the difference between the corresponding terms in the momentum equations for $\langle \bar{v} \rangle$ (6), the tendency terms (WO − TW, solid line), and the bottom stress terms (TW − WO, dashed line). The terms are scaled by the local depth, H.

kinetic energy (TKE) and the vertical eddy dissipation, K_M (Fig. 10).

c. *Tidal effects on the cross-shore transport*

To verify that the internal tide affects the cross-shore and vertical transport on the subtidal temporal scale, we compute the streamfunction ψ_{bc} of the baroclinic velocity field:

$$\psi_{\mathrm{bc}}(x, z, t) = \int_{-H}^{z} u_{\mathrm{bc}}(x, z', t)\, dz'. \tag{7}$$

To obtain time-averaged ψ_{bc} corresponding to subtidal flow, we compute the integral in (7) using u_{bc} at instantaneous depths of vertical levels. Every snapshot of ψ_{bc} is then interpolated to the neutral z levels, corresponding to $\zeta = 0$, and daily averages of the interpolated values are computed.

These are shown for selected days in Fig. 11. Plots on the left correspond to the WO case and are similar to those in Allen et al. (1995). As upwelling progresses, the surface Ekman transport is distributed over a surface boundary layer of increasing thickness. The compensating onshore shelf transport is distributed over the entire water column during the early stages (Fig. 11a). At later stages of upwelling (Figs. 11b–d), the compensating onshore shelf transport becomes more and more concentrated in a thin boundary layer near the bottom. In the TW case (plots on the right in Fig. 11), the cross-shore and vertical transports are affected by the presence of the internal tide. In particular, in the near-bottom area on the midshelf, $H < 100$ m, where the internal tide is intensified, the subtidal onshore transport is distributed

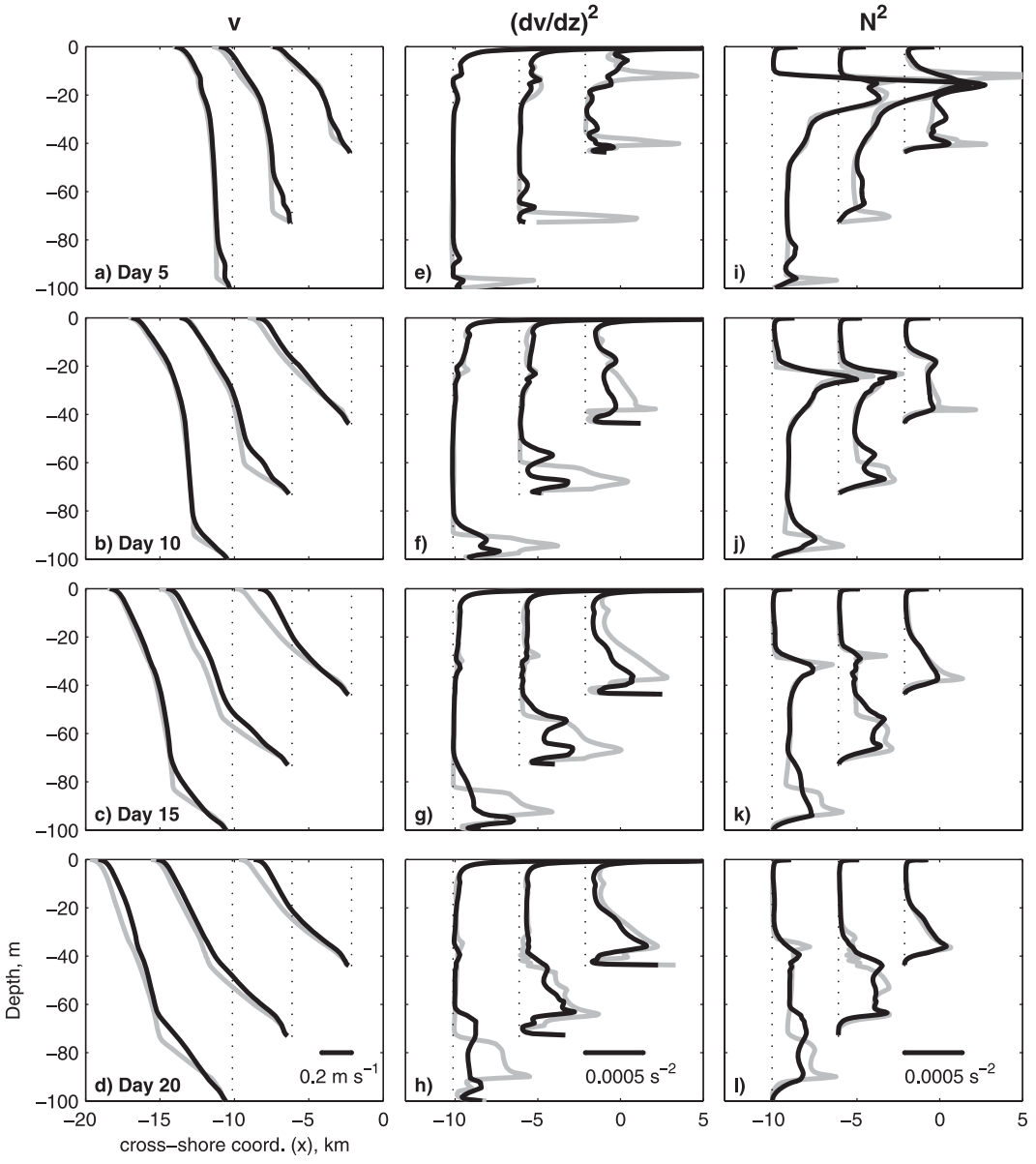

FIG. 9. Profiles of daily averaged subtidal (left) v, (center) $(\partial v/\partial z)^2$, and (right) N^2, for the WO (halftone) and TW (black) cases, in water depths of (44, 73, 100) m, at distances of (2, 6, 10) km from the coast, respectively, on days (top to bottom) 5, 10, 15, and 20.

over a larger layer. Also, local changes in the time-averaged vertical transport are evident along the paths of energetic internal tide beams (particularly apparent between $x = -30$ and -10 km).

A closer look at streamfunctions for day 15, with contours shown at smaller intervals (Fig. 12), reveals differences in the cross-shelf transport in the mid- and inner-shelf areas ($H < 100$ m). For instance, in the TW case the streamfunction lines are relatively more closely spaced in the area $-6 < x < -2$ km at a distance of approximately 20 m from the bottom, indicating an increased cross-shore flow. To confirm this, profiles of daily averaged $\langle u \rangle$, WO (halftone) and TW (black) cases, are shown in Fig. 13a. For this analysis, instantaneous u was projected on neutral (stationary) vertical levels, low-pass filtered, and then averaged over a given time interval. In Fig. 13a, the increased onshore transport in the inner-shelf zone, in the TW case compared to WO, is compensated by the increased offshore transport near the surface. Figure 13b shows the integrated onshore transport, obtained by vertical integration of positive u segments of each profile in Fig. 13a. In the WO

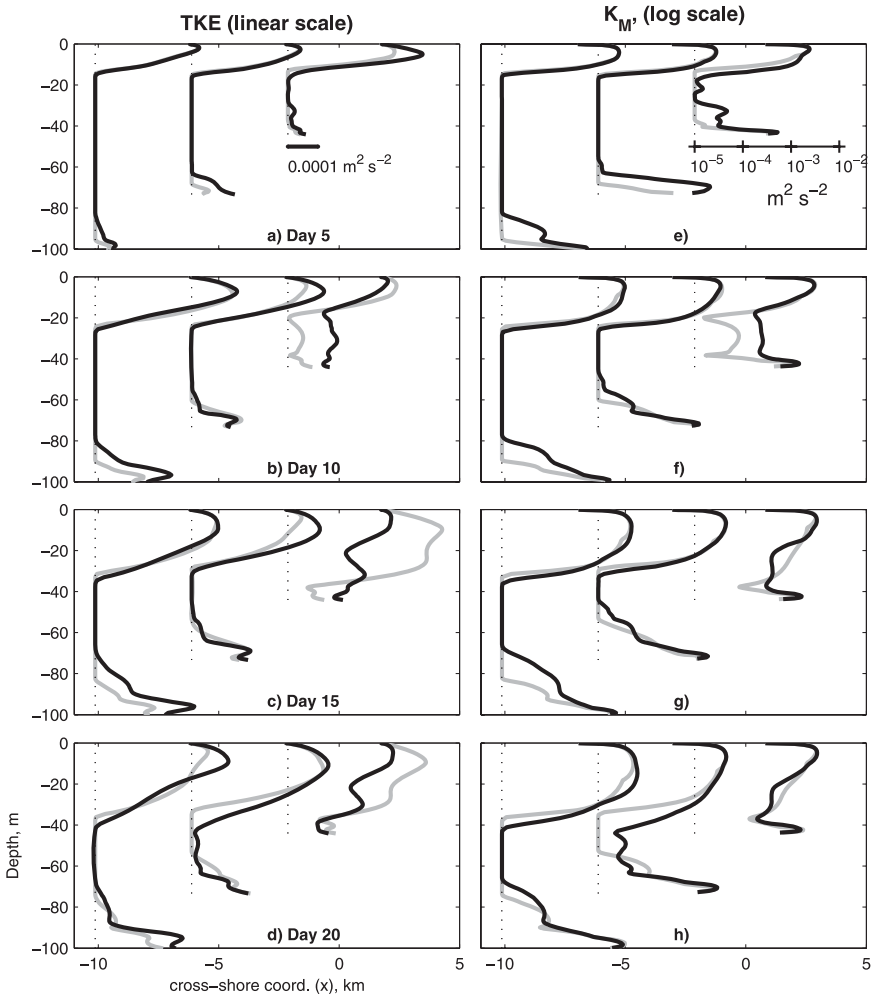

FIG. 10. Profiles of daily averaged (left) TKE and (right) K_M, for the WO (halftone) and TW (black) cases, in water depths of 44, 73, and 100 m, on days (top to bottom) 5, 10, 15, and 20. Note that K_M profiles are shown on the log-10 scale; the reference value of $K_M = 10^{-5}$ m^2 s^{-2} is the minimum background vertical eddy dissipation set in the model.

case, the value corresponding to the cross-shore Ekman transport (approximately 0.5 m^2 s^{-1}) is reached at $x = -15$ km. On average over the shelf area considered, the integrated onshore transport (and consequently the offshore transport) is 25% larger in the TW case than in WO.

The influence of internal tides on the subtidal cross-shore transport is clearly a nonlinear effect. Theoretical studies (e.g., Wunsch 1971) have suggested that the advection associated with baroclinic tidal currents can contribute to the wave-averaged momentum balance over the shelf slope, in the form of the Reynolds stress divergence. To verify the relative importance of this mechanism, we have utilized the ROMS diagnostics and computed the terms on the rhs of the u-momentum equation averaged over $t = (10, 15)$ days (for the technical details of this term balance analysis, see the appendix). The first-order balance is between the Coriolis and pressure gradient terms. In the WO case, as shown in Fig. 14a for the inner shelf location ($x = -3$ km) and Fig. 14c for the midshelf location at $x = -6$ km, the ageostrophic term (an algebraic sum of the Coriolis and pressure gradient terms) is nearly 0 in the middle of the water column and is increased in the surface and bottom boundary layers where it is balanced by the vertical dissipation term. In this case the advection term is near 0. In the TW case, at the same locations (Figs. 14b and 14d), the advection term is not negligible throughout the water column. In the inner shelf area (Fig. 14b; $x = -3$ km) the advection term provides a sizable contribution to the cross-shore momentum balance near the surface, potentially influencing the cross-shore Ekman transport at that location

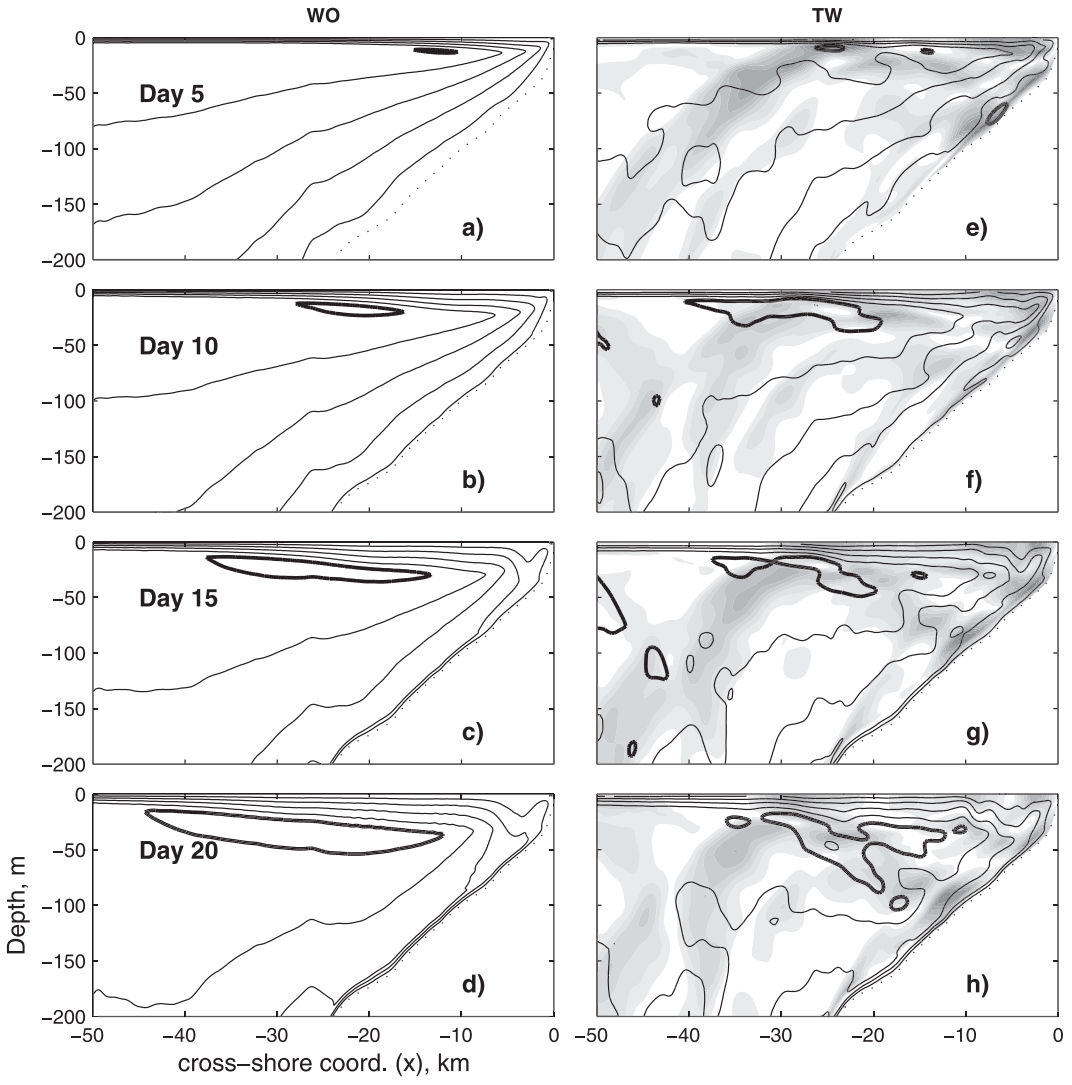

FIG. 11. Cross-shore sections of daily averaged streamfunctions for baroclinic flow, for the (left) WO and (right) TW cases, (top to bottom) averages for days 5, 10, 15, and 20. Contour interval (CI) is 0.1 $m^2\ s^{-1}$; contour 0.5 $m^2\ s^{-1}$ is set in boldface. The shades in the plots on the right are $KE^{1/2}$ of the tidal flow, corresponding to intervals of (top to bottom) (2, 5), (7, 10), (12, 15), and (17, 20), with the same contour spacing as in Fig. 5.

(see Fig. 13). At the midshelf location (Fig. 14d; $x = -6$ km), the advection term is relatively small near the surface and bottom, although it is important in the middle of the water column.

Away from the boundary layers, the cross-shore advection term is balanced by the ageostrophic term over the entire shelf and the advection term contributes to the cross-shelf dynamics in the TW case, much more so than in case WO, as can be seen in a series of profiles of the advection term (halftone) and the combination of the ageostrophic and dissipation terms (black) in Fig. 15.

An estimate of the Reynolds stress divergence component of the total advection [see the appendix, especially (A1)] was obtained by postprocessing the model output, utilizing the same numerical scheme for advection as that in ROMS. We found that the total advection term in the TW case is almost entirely due to the Reynolds stress divergence.

It can also be instructive to look at alongshore momentum term balance profiles, at the same locations, $x = -6$ and -3 km, and averaging interval, $t = (10, 15)$. In the WO case (Figs. 16a and 16b), advection plays an important role in the alongshore direction. In the upper part of the water column the southward jet acceleration (circles) is forced by the turbulent dissipation term. At $x = -3$ km, the advection term works against this force. Note that in this alongshore-uniform case $\partial v/\partial y = 0$ such that only the cross-shore and vertical terms contribute to

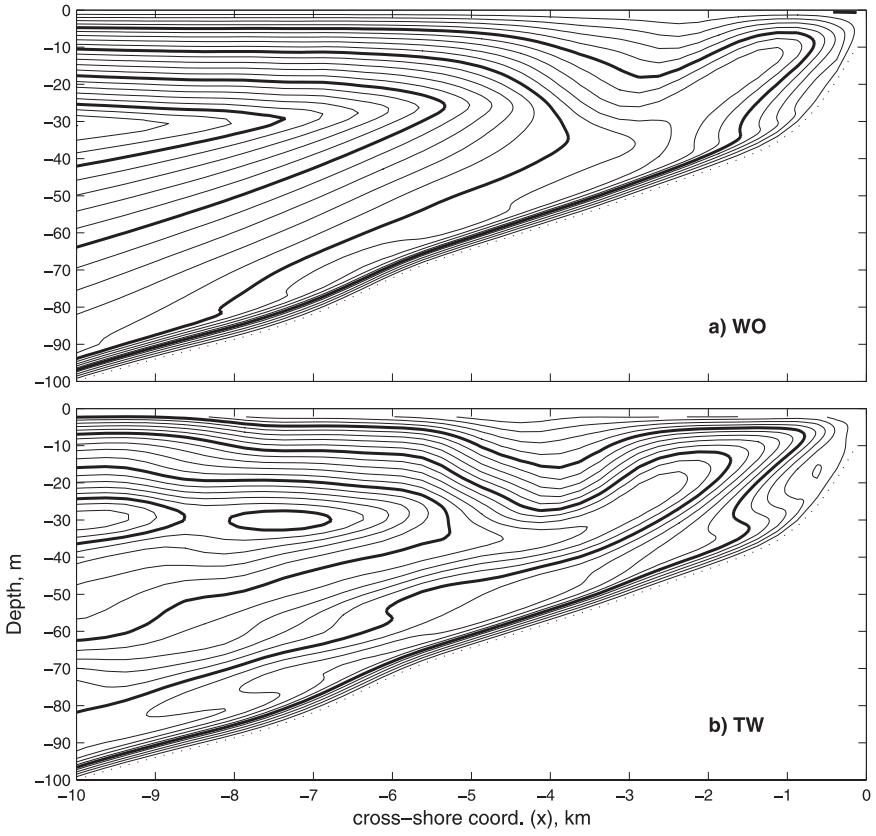

FIG. 12. Sections of daily averaged streamfunctions for baroclinic flow, close-up plots near the coast on day 15, for the (a) WO and (b) TW cases. CI is 0.02 $m^2\ s^{-1}$; boldfaced contours are 0.1, 0.2 $m^2\ s^{-1}$, etc.

the advection. The sign of the alongshore advection term in Fig. 16 is largely determined by the vertical component ($-w\partial v/\partial z > 0$, since $w > 0$ and $\partial v/\partial z < 0$). Also note that since $\partial p/\partial y = 0$, the ageostrophic term is identical to the Coriolis term. The tidal current yields quantitative changes in the term profiles throughout the water column (Figs. 16c and 16d). Below the surface boundary layer, modulations in the advection caused by the nonlinear tidal effect tend to be balanced by corresponding variations in the Coriolis term ($-fu$).

d. *Tidal effects on the turbulence in the boundary layers*

Sections of daily averaged TKE, per unit mass, are shown in Fig. 17, for the WO (top) and TW (bottom) cases, for 0, 10, and 20 days [time intervals of $t = (-1, 0)$, $(9, 10)$, and $(19, 20)$, respectively]. In the WO case, TKE = 0 at the beginning of the run. In the TW case, by the time the wind forcing begins to be applied, the near-bottom TKE is already elevated due to the tidal motion, particularly in the midshelf area where the tidal beam meets the shelf bottom (Fig. 17b). The level of TKE induced by tides in this area is comparable to that associated with the wind-driven circulation at later times. As upwelling develops, the internal tide affects the magnitude and spatial variability of the time-averaged TKE on the inner shelf (Figs. 17c–f), as discussed further below.

In the WO case, instantaneous maps of TKE are very similar to the daily averaged plots. In contrast, in the TW case, the tide causes substantial TKE modulations over a tidal period in both the bottom and surface boundary layers, as seen in Fig. 18, showing snapshot sections of TKE during 0, 10, and 20 days (left, middle, and right columns, respectively). The TKE is elevated not only in the surface layer but in the bottom boundary layer in the presence of tides. Intermittent patches of higher TKE are also found in the ocean interior, separated from the bottom boundary layer. Turbulence in these patches is produced by the combined vertical shear of the wind-driven and tidal horizontal currents. This mechanism was first suggested by Avicola et al. (2007) based on their analysis of hydrographic and turbulence microstructure data. Consistent with their findings, we note that neither

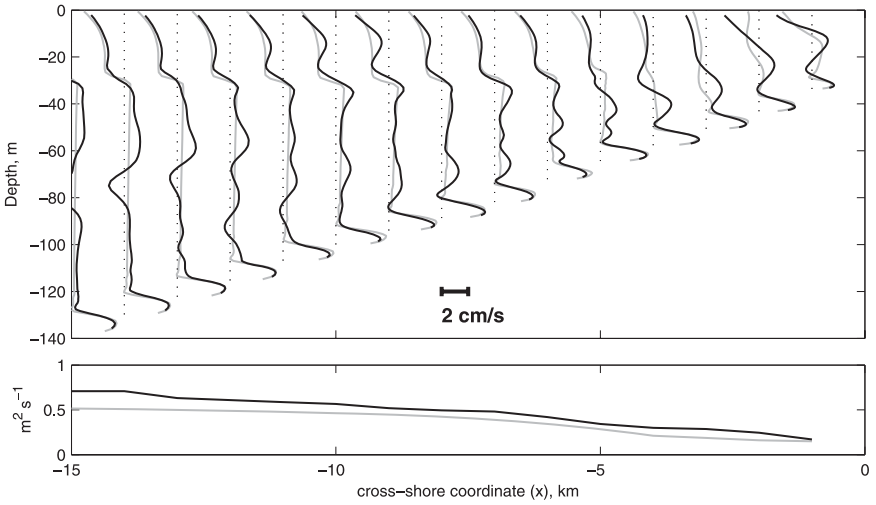

FIG. 13. (a) Vertical profiles of subtidal u, averaged over day 15 and (b) integrated onshore transport (computed using positive segments of the u profiles), for the WO (halftone) and TW (black) cases.

wind-driven shear (in the case of constant wind stress) nor tidally driven shear, acting alone, is enough to overturn the stratification and create the turbulent patches away from the surface and bottom boundary layers. We also note that in the WO case (Fig. 17e), the surface and bottom boundary layers are merged over the inner shelf, forming a vertically continuous TKE front at distances of 2–7 km from the coast, similar to the findings of Wijesekera et al. (2003). In the TW case, the internal tide propagating onto the inner shelf periodically separates the surface boundary layer from the bottom boundary layer, affecting the vertical continuity of the turbulent front (Figs. 18k–o). We note that results for day 20 should be taken with caution since the surface boundary layer thickness is nearly 40 m on this day. This is larger than is generally observed in hydrographic

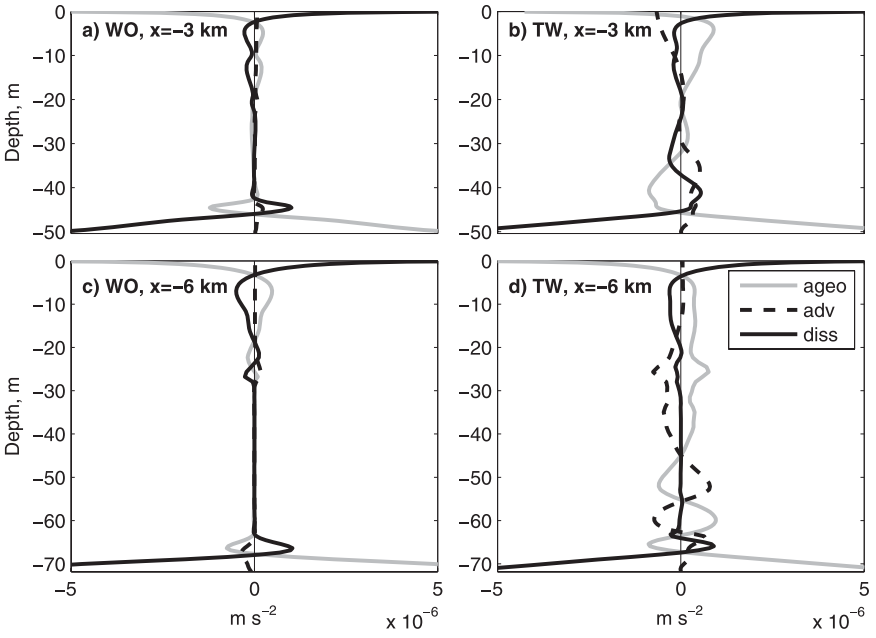

FIG. 14. Vertical profiles of terms (ageostrophic, advection, and vertical dissipation) on the right-hand side of the cross-shore momentum equation averaged over $t = (10, 15)$ days: (top) $x = -3$ km and (bottom) $x = -6$ km, (left) WO, (right) TW.

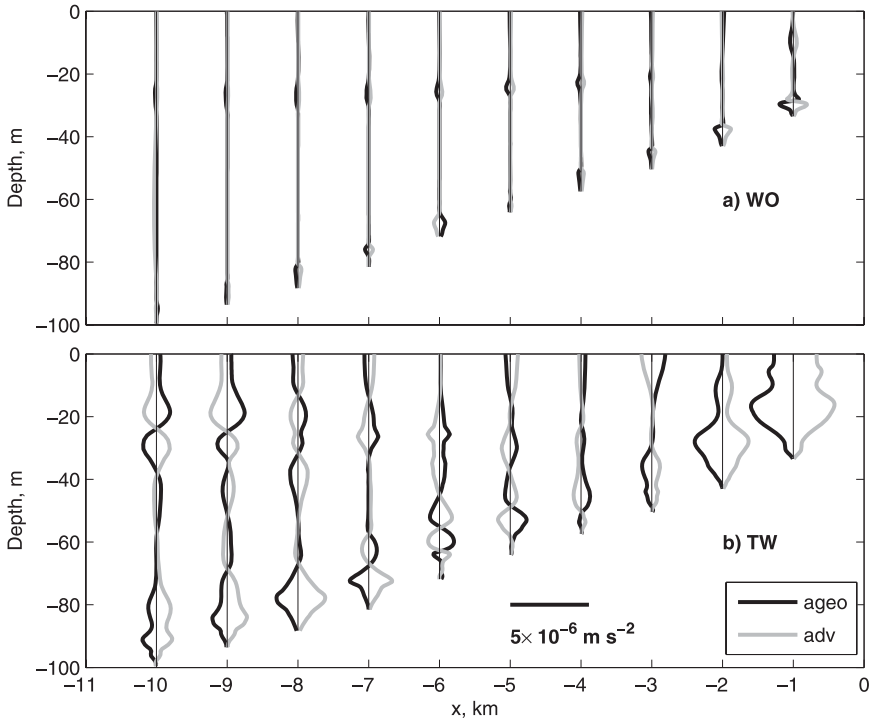

FIG. 15. Vertical profiles of terms (the sum of ageostrophic and dissipation terms in black, advection in halftones) on the right-hand side of the cross-shore momentum equation, averaged over $t = (10, 15)$ days: (a) WO and (b) TW. Thin lines show profile locations and positive values are to the right of these lines.

sections on the mid–Oregon shelf, where occurrences of sustained southward wind stress as strong as 0.05 N m^{-2} are rare.

The internal tide also causes substantial modulations in the surface boundary layer (e.g., cf. the instantaneous section plots in Figs. 6b and 6c). Additional analysis has shown that these modulations are caused by tidal variations in the vertical shear in the alongshore horizontal velocity component. Corrugations in the isopycnals on the vertical scale of 10 m (or larger), similar to those in Figs. 6a and 6c, are commonly found in observed hydrographic sections over the Oregon shelf (Barth et al. 2005).

4. Cases with time variable wind stress

Computations with time-variable wind stress, using observed wind speed time series off the Oregon coast during summer 2001 (Kurapov et al. 2005) were performed to see how robust the results of the previous sections are with a more realistic wind forcing. This also allowed us to check if the intensity of the internal tide, and its effects on subinertial circulation, correlate with the occurrence of upwelling and relaxation events. The tidal forcing is the same as in the previous section. For brevity, we only discuss additional analyses complementary to the previous section.

Time is measured in days since the beginning of the year 2001. The TW case was started from rest at $t = 127$ days and tidally forced for a period of 10 days. At $t = 137$ days, the alongshore wind stress is applied, in addition to the barotropic tidal forcing, and is ramped up from 0 to the observed values over 2 days (Fig. 19a), while the heat flux is ramped up to a constant value of 150 W m^{-2}. The WO case is started from rest at $t = 137$ days, with the same surface forcing.

Time series of the depth-averaged alongshore velocity $\overline{v}$ at locations 10, 6, and, 2 km from the coast are shown in Figs. 19b–d. The internal tide has a relatively larger impact during days 150–170. In particular, at $x = -6$ and -2 km, the current is reduced by nearly 0.1 m s^{-1} (or by approximately 25%). As in the previous section, the reduction in $\overline{v}$ is caused by the increased subtidal bottom stress in the TW case. However, after day 170, the effects of the tides on the subtidal alongshore current are diminished. Also, no apparent correlation between the wind stress and the tidal effect is apparent.

The decreased effects of the internal tide during the later stages of the computational experiment are clarified by analysis of the baroclinic tidal energy balance,

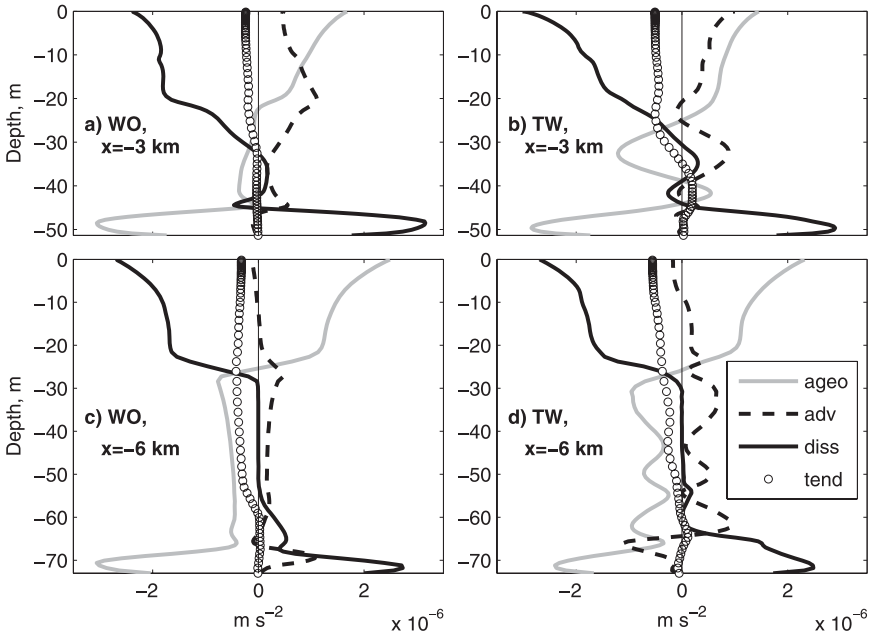

FIG. 16. Similar to Fig. 14, showing terms in the alongshore-shore momentum equation, averaged over t = (10, 15) days. The tendency term is additionally shown as circles (with negative values corresponding to the accelerating southward current). The tendency term is assumed to be on the lhs and all other terms on the rhs of the momentum equation.

based on linear equations [Kurapov et al. (2003), see Eq. (34)]. On average over the tidal period, the divergence in the depth-integrated baroclinic energy flux (F_{int}) is balanced by the topographic energy conversion (EC) and dissipation (DISS), the latter including contributions from bottom friction and turbulence throughout the water column:

$$-\frac{dF_{\text{int}}}{dx} + \text{EC} - \text{DISS} \approx 0, \tag{8}$$

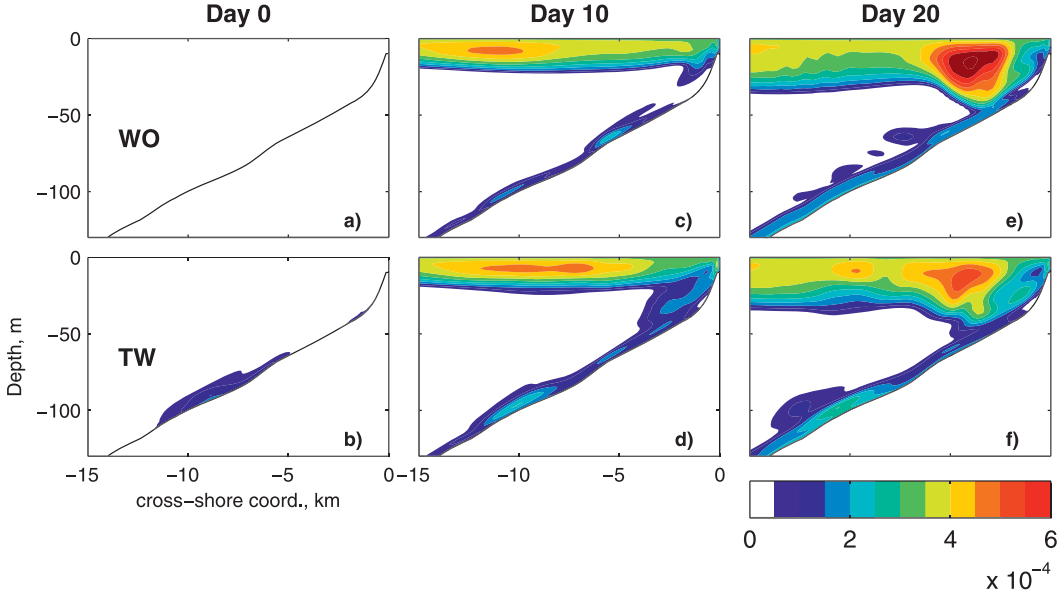

FIG. 17. Daily averaged TKE, CI is 5×10^{-5} m^2 s^{-2}: (top) WO and (bottom) TW for (left to right) days 0, 10, and 20.

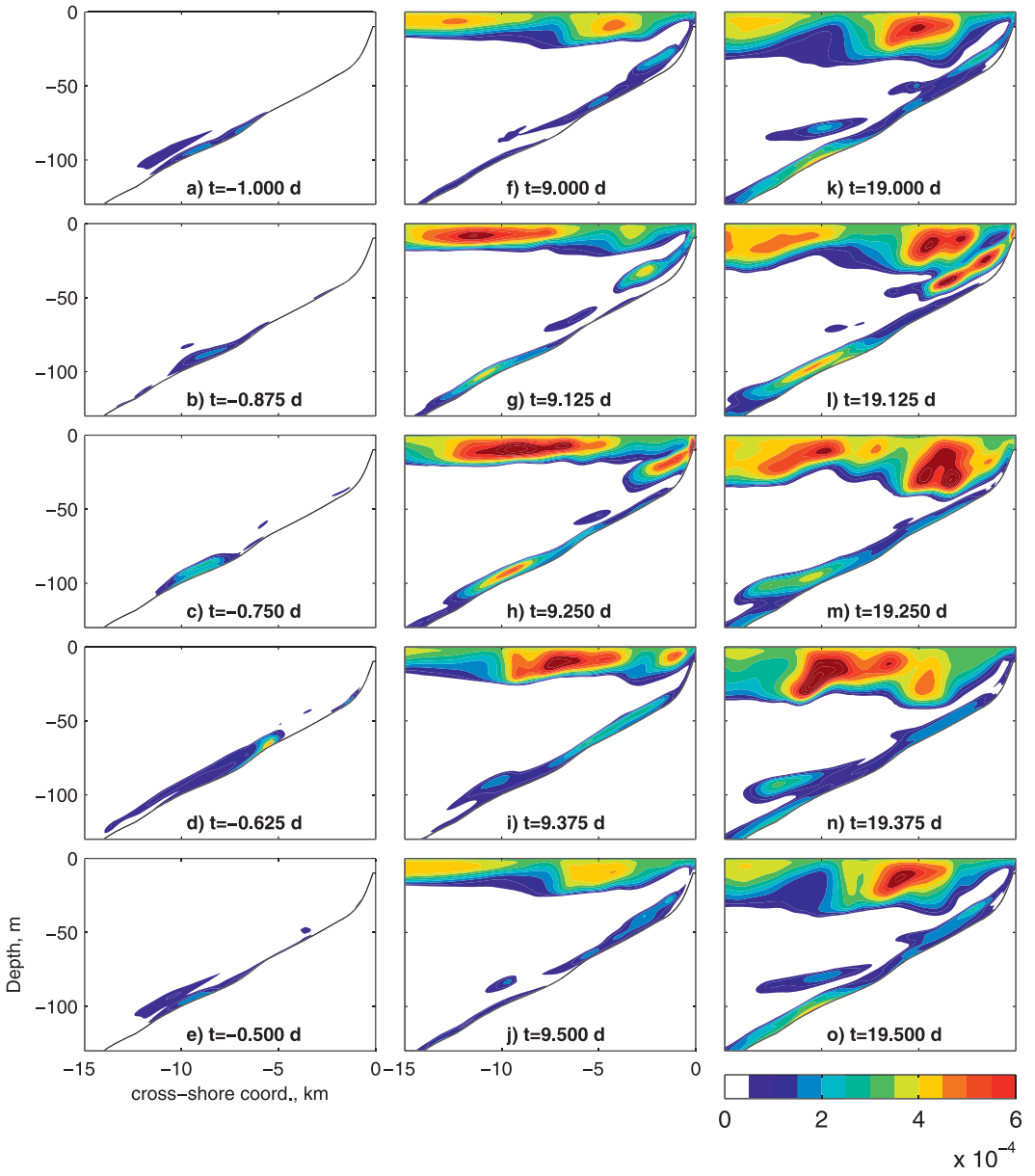

FIG. 18. Instantaneous TKE ($m^2\ s^{-2}$) for the TW case. In each column, the time interval between snapshots is 3 h and snapshots span a period of 12 h: (left) day 0, before atmospheric forcing is applied; (middle) day 10; and (right) day 20.

where

$$F_{\text{int}} = \int_{-H}^{0} F(x, z)\, dz, \tag{9}$$

$$F(x, z) = \text{Re}[\mathbf{u}_{\text{bc}}\mathbf{p}_{\text{bc}}^{\dagger}], \quad \text{and} \tag{10}$$

$$\text{EC} = -\text{Re}[\mathbf{p}_{\text{bc}}|_{\mathbf{z}=-\mathbf{H}}\overline{\mathbf{u}}^{\dagger}]\frac{dH}{dx}, \tag{11}$$

where $F(x, z)$ is the cross-shore component of the tidal horizontal baroclinic energy flux averaged over the tidal period, $\mathbf{p}_{\text{bc}}$ is the baroclinic (total minus depth averaged) tidal pressure, boldface symbols denote tidal complex amplitudes as before (see section 3a), and the dagger symbol denotes a complex conjugate. To compute $\mathbf{p}_{\text{bc}}$, the high-pass-filtered potential density $\sigma_\theta'(x, z, t)$ is harmonically analyzed; the resulting complex amplitude $\boldsymbol{\sigma}_\theta\ (x, z)$ is integrated in the vertical from z to 0 and multiplied by g to obtain the contribution of tidal density variations to the total pressure, and each vertical pressure profile is demeaned.

Figure 20 shows cross sections of the tidal baroclinic energy flux $F(x, z)$ (top panels), the vertically integrated flux F_{int} (middle panels), and—dF_{int}/dx (black), EC

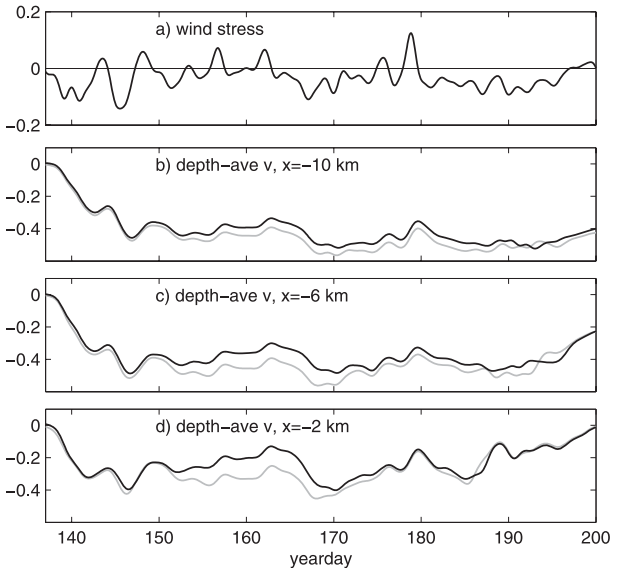

FIG. 19. Time series of (a) wind stress, and (b)–(d) $\langle \bar{v} \rangle$ at distances of 10, 6, and 2 km from the coast, for cases with the time-variable wind stress: TW (black) and WO (halftone).

(halftone), and the residual dF_{int}/dx—EC (red) (bottom panels). The residual is largely negative and can be associated with the term DISS in (8). Plots from left to right correspond to different intervals over which a harmonic analysis was performed. During the period when only tidal forcing was applied, $t = (134, 137)$, the barotropic-to-baroclinic energy conversion occurred mainly over the continental slope, within the range of $H = 400$–1000 m (Fig. 20c). This conversion is balanced by the energy flux divergence term, with very little residual (dissipation). Approximately the same amount of energy is radiated in both directions, toward the open ocean and onto the shelf (Figs. 20a and 20b). On the shelf ($x > -30$ km, $H < 200$ m), the energy flux is decreased toward the coast, due to dissipation. During the period of increased tidal influence on the alongshore transport, $t = (150, 160)$ (Figs. 20d–f), EC at the continental slope is reduced compared to the previously discussed interval, although a significant flux is still directed onshore. Additional topographic energy conversion occurs in the vicinity of the shallow bathymetric feature at $x = -30$ km. For the interval $t = (180, 190)$ (Figs. 20g–i), when the tidal effect on the alongshore transport is reduced, the energy flux directed from the continental slope onshore is very low. The barotropic-to-baroclinic energy conversion over the shallow topographic feature near $x = -30$ km is larger than at the earlier time, increasing the onshore flux at depths $H <$ 200 m, although only about half of the baroclinic tidal energy generated in that area is radiated and the rest is dissipated locally. We also note that the magnitude of F_{int} (see Figs. 20b, 20e, and 20h), ≤ 20 W m^{-1}, is comparable to the estimates obtained for the mid–Oregon shelf in a 3D model constrained by assimilation of HF radar surface currents (Kurapov et al. 2003).

Note that in the three time windows discussed in the previous paragraph, the magnitude of the onshore integrated flux is more affected by the background conditions than the offshore flux (see Figs. 20b, 20e, and 20h). Also note that the reduction in the integrated flux magnitudes at depths $H > 200$ m is not associated with dissipation, since in those areas the flux divergence is well balanced by EC. Without the wind forcing, the bathymetric slope at $400 < H < 1000$ m is very close to critical, such that M_2 characteristic slopes (5) are nearly parallel to the bathymetric slope (see characteristic slope lines in Fig. 20a). With the development of upwelling, the near-bottom background stratification over the slope is increased such that the characteristic slopes become less steep (see Figs. 20d and 20g). The slope becomes increasingly supercritical, reducing the efficiency of the baroclinic energy conversion on this slope, and radiating a larger fraction of the available baroclinic energy into the open ocean. Note that in this analysis, the buoyancy frequency was computed using density values in the two lowest layers. Of course, in addition to this interpretation, other mechanisms can be suggested to explain the internal tide intermittency.

5. Summary

We have demonstrated that a moderate internal tide, with currents of 10–15 cm s^{-1} amplitude, can influence alongshore and cross-shore transports on subinertial time scales, in part through modifications of the bottom boundary layer. The divergence in the tidally induced Reynolds stress contributes to the cross-shore momentum balance on the shelf and can affect the subtidal cross-shore transport in the middle of the water column. No simple relationship was found between wind stress fluctuations and tidal energetics or tidal effects on the subtidal flow.

Our study has confirmed that variability in the background conditions associated with wind-driven upwelling can cause substantial intermittency in the internal tide on the continental shelf. Changes in the background stratification over the continental slope associated with upwelling are sufficient to change the classification of the slope to subcritical, critical, or supercritical, providing control on the amount of barotropic-to-baroclinic energy conversion and the preferred direction of baroclinic energy flux (offshore or onshore).

The assumption that flows are alongshore uniform is a limitation of this idealized study. In particular,

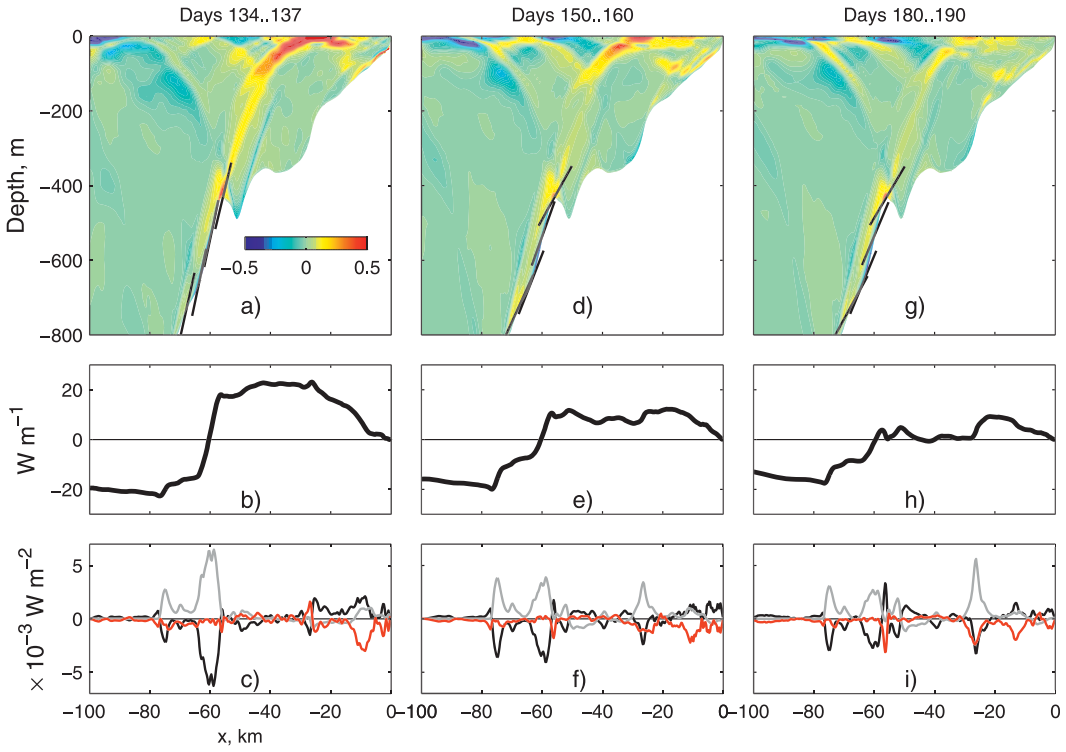

FIG. 20. Baroclinic tidal energy analysis for the case with time-variable wind, estimated using harmonic analysis over intervals (left to right) t = (134, 137) (tide only), (150, 160), and (180, 190). (top) The baroclinic energy flux $F(x, z$; W m^{-2}); black lines show the M_2 characteristic slope near the bottom at a number of locations on the continental slope; (middle) the depth-integrated baroclinic energy flux F_{int}; and (bottom) the depth-integrated baroclinic tidal energy balance terms including the energy flux convergence—$\partial F_{\text{int}}/\partial x$ (black), the topographic energy conversion term EC (halftone), and the residual $\partial F_{\text{int}}/\partial x$—EC, interpreted as the dissipative term (red).

superinertial waves are essentially 3D features that can propagate at angles oblique to the coastline. Clearly, similar analyses with a high-resolution 3D model should be pursued. However, the effects of the internal tide in decreasing the subtidal alongshore current speed will be more difficult to analyze in the 3D setup because differences between the WO and TW solutions may result from alongshore pressure gradients and other alongshore variable conditions set up in the model interior. In the 2D formulation adopted here, such complications are eliminated and it is clearly demonstrated that the changes in the alongshore momentum are associated with increased bottom friction.

The intermittent internal tide is difficult to analyze using traditional oceanographic observations. For instance, inferences from a single mooring (or a sparse array of moorings) about the internal tide energetics, particularly its dependency on background ocean conditions, can be misleading since the zones of most intense activity move around. HF radar observations provide opportunities to obtain spatial maps of tidal surface velocities (O'Keefe 2005) and these can be utilized to verify model predictions or constrain the model estimates by means of data assimilation (Kurapov et al. 2003; Zaron et al. 2009). The modeling approach provides unique opportunities to understand the structure and dynamical role of the internal tide in the coastal ocean. To adequately represent the variability in the internal tide, these models must include realistically changing background conditions.

Acknowledgments. The research was supported by the National Science Foundation (NSF) under Grant OCE-0648314 and by the Office of Naval Research (ONR) Physical Oceanography Program under Grant N00014-08-1-0942.

APPENDIX

Details of $\langle u \rangle$-Momentum Balance Computation

The u-momentum equation in terrain-following s coordinates, with the low-pass filter applied to each term, is

$$\frac{\partial\langle H_z u\rangle}{\partial t} = \mathrm{Adv}[\langle U\rangle, \langle u\rangle, \langle\Omega\rangle] + \langle \mathrm{Adv}[U', u', \Omega']\rangle - \left\langle \frac{H_z}{\rho_0}\frac{\partial p}{\partial x}\bigg|_z \right\rangle + \langle H_z f v\rangle + \left\langle \frac{\partial}{\partial s}\left(\frac{K_M}{H_z}\frac{\partial u}{\partial s}\right)\right\rangle, \tag{A1}$$

where

$$\mathrm{Adv}[U, u, \Omega] = -\frac{\partial(Uu)}{\partial x} - \frac{\partial(\Omega u)}{\partial s}, \tag{A2}$$

$H_z = \partial z/\partial s$, $U = H_z u$, and where Ω is the velocity component normal to the s coordinates, as defined in ROMS (Shchepetkin and McWilliams 2005). Note that in the discretized equations, H_z is the layer thickness, which varies with time. The terms on the rhs of Eq. (A1) are (left to right) the advection by the subtidal current, the Reynolds stress divergence, the pressure gradient term (written in shorthand notation where the subscript z is used to emphasize that the derivative is taken in the horizontal direction), the Coriolis term, and the vertical dissipation term (with the vertical eddy dissipation K_M determined internally in ROMS, based on the turbulence parameterization). The total advection term is the sum of the first two terms of the rhs of (A1).

At each time step in ROMS, the instantaneous momentum terms are scaled by H_z point by point, to obtain units of meters per second squared, averaged over prescribed time intervals, and written to the output file. Since ROMS does not provide diagnostics separately for the Reynolds stress component of the advection, we computed this term, and additionally other terms in (A1), by postprocessing the instantaneous hourly outputs, using the same discretization scheme as in ROMS. The terms were low-pass filtered, averaged over a specified time interval in s coordinates, and then scaled by the thickness of the unperturbed grid cells (corresponding to $\zeta = 0$). We have verified that the advection (the sum of the two components) and the other terms obtained by the postprocessing process are close to the time-averaged ROMS diagnostics.

REFERENCES

Allen, J. S., and P. A. Newberger, 1996: Downwelling circulation on the Oregon continental shelf. Part I: Response to idealized forcing. *J. Phys. Oceanogr.,* **26,** 2011–2035.

——, ——, and J. Federiuk, 1995: Upwelling circulation on the Oregon continental shelf. Part I: Response to idealized forcing. *J. Phys. Oceanogr.,* **25,** 1843–1866.

Avicola, G., J. N. Moum, A. Perlin, and M. D. Levine, 2007: Enhanced turbulence due to the superposition of internal gravity waves and a coastal upwelling jet. *J. Geophys. Res.,* **112,** C06024, doi:10.1029/2006JC003831.

Baines, P. G., 1982: On internal tide generation models. *Deep-Sea Res.,* **29,** 307–338.

Barth, J. A., S. D. Pierce, and R. M. Castelao, 2005: Time-dependent, wind-driven flow over a shallow mid-shelf submarine bank. *J. Geophys. Res.,* **110,** C10S05, doi:10.1029/2004JC002761.

Chen, D., H. W. Ou, and C. Dong, 2003: A model study of internal tides in coastal frontal zone. *J. Phys. Oceanogr.,* **33,** 170–187.

Erofeeva, S. Y., G. D. Egbert, and P. M. Kosro, 2003: Tidal currents on the central Oregon shelf: Models, data, and assimilation. *J. Geophys. Res.,* **108,** 3148, doi:10.1029/2002JC001615.

Federiuk, J., and J. S. Allen, 1995: Upwelling circulation on the Oregon continental shelf. Part II: Simulations and comparisons with observations. *J. Phys. Oceanogr.,* **25,** 1867–1889.

Flather, R. A., 1976: A tidal model of the north-west European continental shelf. *Mem. Soc. R. Sci. Liège,* **6,** 141–164.

Gan, J., J. S. Allen, and R. M. Samelson, 2005: On open boundary conditions for a limited-area coastal model off Oregon. Part II: Response to wind forcing from a regional mesoscale atmospheric model. *Ocean Modell.,* **8,** 155–173, doi:10.1016/j.ocemod.2003.12.007.

Gill, A. E., 1982: *Atmosphere–Ocean Dynamics*. Academic Press, 662 pp.

Hall, P., and A. M. Davies, 2007: Internal tide modeling and the influence of wind effects. *Cont. Shelf Res.,* **27,** 1357–1377, doi:10.1016/j.csr.2006.09.008.

Hayes, S. P., and D. Halpern, 1976: Observations of internal waves and coastal upwelling off the Oregon coast. *J. Mar. Res.,* **34,** 247–267.

Holloway, P. E., 2001: A regional model of the semi-diurnal internal tide on the Australian North Shelf. *J. Geophys. Res.,* **106,** 19 625–19 638.

Kurapov, A. L., G. D. Egbert, J. S. Allen, R. N. Miller, S. Y. Erofeeva, and P. M. Kosro, 2003: M_2 internal tide off Oregon: Inferences from data assimilation. *J. Phys. Oceanogr.,* **33,** 1733–1757.

——, J. S. Allen, G. D. Egbert, and R. N. Miller, 2005: Modeling bottom mixed layer variability on the mid-Oregon shelf during summer upwelling. *J. Phys. Oceanogr.,* **35,** 1629–1649.

Lentz, S. J., and J. H. Trowbridge, 1991: The bottom boundary layer over the northern California shelf. *J. Phys. Oceanogr.,* **21,** 1186–1201.

MacCready, P., and P. B. Rhines, 1993: Slippery bottom boundary layers on a slope. *J. Phys. Oceanogr.,* **23,** 5–22.

Mellor, G. L., and T. Yamada, 1982: Development of a turbulence closure model for geophysical fluid problems. *Rev. Geophys. Space Phys.,* **20,** 851–875.

Mooers, C. N. K., 1970: The interaction of an internal tide with the frontal zone of a coastal upwelling region. Ph.D. thesis, Oregon State University, 480 pp.

——, 1975a: Several effects of a baroclinic current on the cross-stream propagation of inertial-internal waves. *Geophys. Astrophys. Fluid Dyn.,* **6,** 245–275.

——, 1975b: Several effects of baroclinic currents on the three-dimensional propagation of inertial-internal waves. *Geophys. Astrophys. Fluid Dyn.,* **6,** 277–284.

Oke, P. R., J. S. Allen, R. N. Miller, and G. D. Egbert, 2002: A modeling study of the three-dimensional continental shelf circulation off Oregon: Part II. Dynamical analysis. *J. Phys. Oceanogr.,* **32,** 1383–1403.

O'Keefe, S., 2005: Observing the coastal ocean with HF radar. M.S. thesis, College of Oceanic and Atmospheric Sciences, Oregon State University, 103 pp.

Park, J.-H., and D. R. Watts, 2006: Internal tides in the southwestern Japan/East Sea. *J. Phys. Oceanogr.,* **36,** 22–34.

Pereira, A. F., B. M. Castro, L. Calado, and I. C. A. da Silveira, 2007: Numerical simulation of M_2 internal tides in the South Brazil Bight and their interaction with the Brazil Current. *J. Geophys. Res.,* **112,** C04009, doi:10.1029/2006JC003673.

Rooth, C., 1972: A linearized bottom friction law for large-scale oceanic motions. *J. Phys. Oceanogr.,* **2,** 509–510.

Shchepetkin, A. F., and J. C. McWilliams, 2005: The Regional Ocean Modeling System: A split-explicit, free-surface, topography-following-coordinate oceanic model. *Ocean Modell.,* **9,** 347–404, doi:10.106/j.oceanmod.2004.08.002.

Smith, R. L., A. Huyer, and J. Fleischbein, 2001: The coastal ocean off Oregon from 1961 to 2000: Is there evidence of climate change or only of Los Niños? *Prog. Oceanogr.,* **49,** 63–93.

Springer, S. R., R. M. Samelson, J. S. Allen, G. D. Egbert, A. L. Kurapov, R. N. Miller, and J. C. Kindle, 2009: A nested grid model of the Oregon coastal transition zone: Simulations and comparisons with observations during the 2001 upwelling season. *J. Geophys. Res.,* **114,** C02010, doi:10.1029/2008JC004863.

Torgrimson, G. M., and B. M. Hickey, 1979: Barotropic and baroclinic tides over the continental slope and shelf off Oregon. *J. Phys. Oceanogr.,* **9,** 945–961.

Wijesekera, H. W., J. S. Allen, and P. A. Newberger, 2003: Modeling study of turbulent mixing over the continental shelf: Comparison of turbulent closure schemes. *J. Geophys. Res.,* **108,** 3103, doi:10.1029/2001JC001234.

Wunsch, C., 1971: Note on some Reynolds stress effects of internal waves on slopes. *Deep-Sea Res.,* **18,** 583–591.

Zaron, E. D., C. Chavanne, G. D. Egbert, and P. Flament, 2009: Baroclinic tidal generation in the Kauai Channel inferred from high-frequency radio Doppler current meters. *Dyn. Atmos. Oceans,* **48,** 93–120.